Journal of Materials Research and Technology 42 (2026) 7956–7971

Contents lists available at ScienceDirect

Journal of Materials Research and Technology

journal homepage: www.elsevier.com/locate/jmrt

Yttrium improves Mg ductility by enhancing grain-boundary strain compatibility: Mesoscopic deformation analysis

Myeong-heom Park [a,*], Binxuan Sun [a], Saho Yako [a], Akinobu Shibata [b], Nobuhiro Tsuji [a]

[a] Department of Materials Science and Engineering, Kyoto University, Yoshida Honmachi, Sakyo-ku, Kyoto, 606-8501, Japan
[b] Research Center for Structural Materials, National Institute for Materials Science (NIMS), 1-2-1 Sengen, Tsukuba, 305-0047, Japan

ARTICLE INFO

Keywords:
Mg alloy
Mechanical properties
Digital image correlation (DIC)
Surface topography
Slip systems
Local deformation behavior

ABSTRACT

Magnesium (Mg) alloys are attractive lightweight structural materials owing to their low density and high specific strength. However, their widespread application is limited by inherently low tensile ductility at room temperature, which is closely related to limited formability. This limitation is primarily attributed to the insufficient activation of non-basal slip systems at room temperature. The addition of Yttrium (Y) has been reported to promote non-basal slip activity, leading to improved mechanical performance. In this study, the mechanisms of ductility enhancement in Mg–Y alloys are investigated from the perspective of mesoscopic deformation behavior using digital image correlation (DIC) combined with careful identical-area observations during tensile deformation. Pure Mg and Mg–1.3Y (at.%) were systematically examined. DIC strain mapping demonstrated that both materials exhibited pronounced deformation heterogeneity, characterized by strain localization in specific grains with relatively high Schmid factor. Notably, the two materials exhibited markedly different grain-boundary deformation behaviors. In pure Mg, severe surface steps and early formation of microcrack-like features were observed at grain boundaries, whereas such damage was significantly suppressed in the Mg–1.3Y alloy. These results indicate that improved strain compatibility and mitigation of grain-boundary surface steps play a critical role in enhancing the tensile ductility of Mg–Y alloys.

1. Introduction

Light metals have attracted increasing attention for structural applications in vehicles and aircraft because of their potential to improve fuel efficiency through weight reduction. Among them, magnesium (Mg) and its alloys possess the lowest density among structural metals (approximately 1.74 g cm^{-3}) and have therefore been extensively investigated as candidate lightweight materials. However, their widespread application remains limited by inherently poor tensile ductility, which is closely associated with limited formability at room temperature.

This limitation originates from the crystallographic constraint of the hexagonal close-packed (HCP) structure, in which plastic deformation is primarily accommodated by (0001)⟨11-20⟩ basal slip. This limited availability of active slip systems fails to satisfy the von-Mises criterion, which requires at least five independent slip systems for arbitrary plastic deformation in polycrystalline materials. Consequently, promoting the activation of non-basal slip systems is widely recognized as an effective approach to improving the tensile ductility of Mg alloys, with implications for formability. Alternative strategies have been explored, such as the fabrication of dual-texture structures [1] and bimodal grain structures [2,3], which aim to improve mechanical properties through microstructural design. Solute addition to the Mg matrix has also been widely employed to modify deformation behavior and enhance ductility [4].

In addition to dislocation slip, deformation twinning can also contribute to ⟨c+a⟩ deformation modes in Mg alloys [1,5–12]. Twinning is strongly dependent on crystallographic orientation; for example, tensile twinning is preferentially activated when the tensile axis is aligned with the c-axis or when the compression axis is perpendicular to the basal plane [11,12]. However, twinning alone does not generally result in a simultaneous improvement in strength and ductility [6]. Instead, twinning often leads to characteristic mechanical responses such as a low yield stress, the appearance of a stress plateau, and delayed work hardening [6,11].

Rare-earth (RE) alloying, particularly with Y and Gd, has been reported to promote the activation of non-basal ⟨c+a⟩ slip in Mg, leading to remarkable improvements in mechanical properties [13–19].

* Corresponding author.
E-mail address: park.myeongheom.8r@kyoto-u.ac.jp (M.-h. Park).

https://doi.org/10.1016/j.jmrt.2026.05.107
Received 20 January 2026; Received in revised form 18 April 2026; Accepted 10 May 2026
Available online 12 May 2026
2238-7854/© 2026 The Authors. Published by Elsevier B.V. This is an open access article under the CC BY license (http://creativecommons.org/licenses/by/4.0/).

Somekawa et al. [20] demonstrated that Y additions in the range of 0.1–2.0 at.% significantly enhanced mechanical properties and directly identified ⟨c+a⟩ dislocations through transmission electron microscopy (TEM) observations. In addition, grain-boundary segregation of Y was observed [21,22], suggesting that solute segregation at the grain boundary may also contribute to ductility enhancement. Accordingly, the activation of non-basal slip and Y-induced modification of grain-boundary characteristics have been widely discussed as important factors governing the improved plastic response of Mg–Y alloys.

In addition to these mechanisms, recent studies have highlighted the potential importance of grain-boundary-related deformation processes and strain accommodation in governing the mechanical response of Mg alloys. In particular, interactions among slip, twins, and grain boundaries, as well as strain accommodation at grain boundaries, have been identified as factors influencing deformation heterogeneity and damage evolution [23–25]. These studies consistently demonstrate that the improvement in ductility of Mg alloys is closely associated with the enhanced activation of non-basal slip systems, often facilitated by solute additions, grain refinement, and boundary-related effects such as twin-boundary interactions and segregation. While these mechanisms are primarily discussed from the perspective of dislocation activity and its modification, they also imply that deformation processes at or near grain boundaries can influence local strain accommodation. Therefore, in addition to intragranular slip activity, the manner in which strain is accommodated and transferred across grain boundaries is considered to play an important role in governing deformation heterogeneity and fracture behavior in Mg alloys.

Although the improvement in ductility of Mg–RE alloys has often been attributed to the activation of non-basal ⟨c+a⟩ slip and, in some cases, to grain-boundary segregation of solute elements, the relative importance of these mechanisms remains under debate. In particular, it is unclear whether the enhanced ductility is primarily governed by changes in dislocation activity at the microscopic scale or by improved strain accommodation and strain compatibility at grain boundaries at the mesoscale. Previous studies have demonstrated that Y can segregate to grain boundaries in Mg–Y alloys [26–28], and such segregation may influence grain-boundary-mediated deformation and fracture behavior [29]. In addition, Y-segregated grain boundaries have been reported to act as nucleation sites for non-basal dislocations [30], suggesting that Y segregation may contribute to ductility enhancement by facilitating local strain accommodation near grain boundaries. Direct visualization and quantitative assessment of strain distribution and the damage across grains are therefore essential for elucidating the underlying origin of global ductility enhancement in Mg–Y alloy.

Digital image correlation (DIC) has recently emerged as an effective technique for investigating local deformation behavior and strain heterogeneity in metallic materials [31–39]. In particular, the DIC analysis enables quantitative assessment of strain partitioning and deformation localization at the microstructural scale, providing complementary information to slip-trace analysis and EBSD-based characterization. Moreover, three-dimensional (3D) surface topography techniques [40,41], which enable quantitative measurement of surface steps and depth variations, offer additional insight into grain-boundary damage evolution during deformation.

In the present study, the tensile properties and local deformation behavior of a Mg–1.3Y alloy are systematically investigated in comparison with those of pure Mg using DIC-based mesoscopic analysis combined with 3D surface topography measurements. By combining observations from mesoscopic strain mapping and surface topography analysis, this study provides new insight into the role of grain-boundary strain compatibility in contributing to the ductility of Mg–Y alloys.

2. Experimental procedures

2.1. Material preparation and microstructural control

Pure Mg (99.9% purity) and a Mg–1.3 at.% Y alloy were used in this study. Hot-extruded pure Mg was employed as the starting material, whereas the Mg–1.3Y alloy was first homogenized at 500 °C for 120 min and subsequently water-quenched. Both materials were then subjected to multi-pass hot rolling at 400 °C with a total thickness reduction of 80% (from 10 mm to 2 mm). To obtain fully recrystallized microstructures with comparable grain sizes, pure Mg was annealed at 400 °C for 30 s, while the Mg–1.3Y alloy was annealed at 500 °C for 60 s in a box furnace, followed by water quenching.

2.2. Microstructure observations

The samples were mechanically polished using SiC abrasive papers with grit sizes ranging from #400 to #4000, followed by final polishing with a 1 μm diamond paste and a 0.04 μm colloidal silica (SiO_2) suspension. Microstructural observations were performed using a field-emission scanning electron microscope (FE-SEM; JSM-7100, JEOL) equipped with an electron backscatter diffraction (EBSD) system operated at an accelerating voltage of 15 kV. The acquired EBSD data were analyzed using TSL Solutions software (TSL-OIM Data Collection, version 7).

Identical-area EBSD analyses were conducted during tensile deformation. {10–12}⟨10–11⟩ tension twins were identified based on a characteristic misorientation angle of approximately 86.3° relative to the parent matrix. Microstructures were observed from the normal direction (ND) and transverse direction (TD) of the rolled sheets, depending on the purpose of the analysis. In particular, the transverse direction (TD) plane was prepared by careful manual polishing using SiC abrasive papers, followed by diamond paste and colloidal silica suspension. During polishing, the specimen was held by hand to ensure uniform material removal and a sufficiently flat and smooth surface for reliable observation of basal (0001) slip traces on the TD plane. This approach was adopted because the strong basal texture limited the visibility of (0001) slip traces when observed from the normal direction (ND). The average grain size was estimated using the line-intercept method based on EBSD grain-boundary maps.

2.3. Tensile properties

Mechanical properties were evaluated by uniaxial tensile testing at room temperature using a universal testing machine (AG-100kN Xplus, Shimadzu) at a quasi-static strain rate of 8.3×10^{-4} s^{-1}. Tensile specimens with a gauge length of 10 mm, a gauge width of 2.0 mm, and a thickness of 2.0 mm were machined by electrical discharge wire cutting (HS-70A, Brother). The tensile axis was aligned parallel to the rolling direction (RD) of the sheets.

Tensile strain was measured using the digital image correlation (DIC) method with commercial strain-visualization software (Vic-2D, Correlated Solutions). Prior to testing, a random speckle pattern was applied to the specimen surface. During deformation, digital images with a resolution of 2432 × 2054 pixels were sequentially captured using a CMOS camera at a constant frame rate of 5 fps and subsequently used for DIC analysis.

2.4. Characterization of local deformation behavior in microstructures

Local deformation behavior was characterized by combined SEM observations and microscopic digital image correlation (μ-DIC) strain analysis. To achieve high spatial resolution in the DIC measurements, the polished specimen surface was patterned using 0.04 μm-sized colloidal silica (SiO_2) particles, as illustrated in Fig. 1. The average interparticle spacing was estimated to be approximately 0.2 μm. For

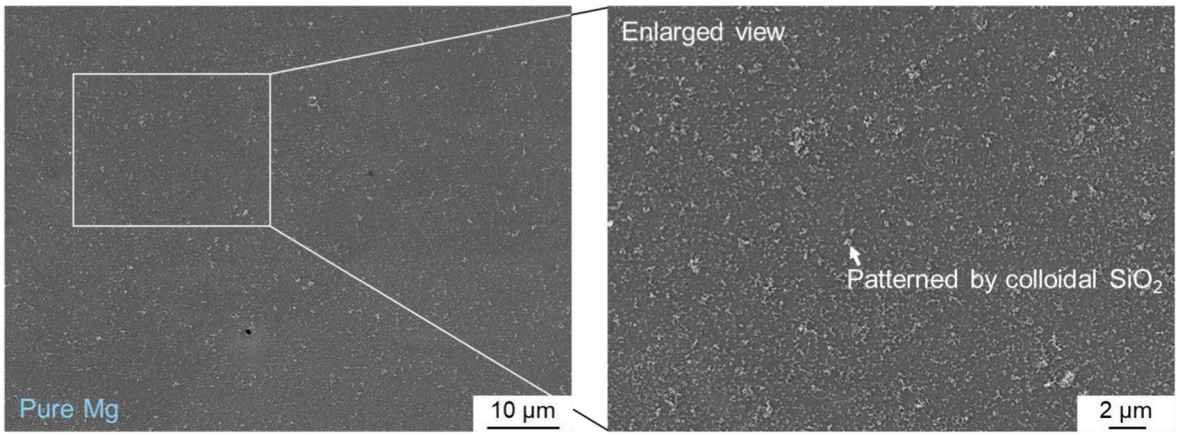


Fig. 1. Preparation of a random speckle pattern using colloidal silica (SiO_2) on the polished surface of the pure Mg specimen for precise local strain analysis by the digital image correlation (DIC) technique.

μ-DIC analysis, forty high-magnification SEM images were acquired and merged into a single montaged image to obtain an overall field of view covering approximately 160-200 grains. This approach enabled detailed analysis of strain distribution within individual grain interiors as well as deformation interactions across neighboring grain boundaries. Each SEM image had a resolution of 1280 × 1024 pixels. The subset size and strain calculation step were set to 43 × 43 pixels (2.65 μm × 2.65 μm) and 7 pixels (0.43 μm), respectively, for both specimens. The resulting random particle distribution provided a reliable speckle pattern for accurate tracking of local displacement and strain fields. The crystallographic orientation of the initial microstructure was determined by EBSD analysis to examine the relationship between activated slip systems and strain localization.

In addition, surface depth variations, particularly near grain boundaries, were evaluated by reconstructing three-dimensional surface profiles. SEM images acquired at tilt angles of −5°, 0°, and +5° relative to the incident electron beam were analyzed using a three-dimensional surface topography measurement system (Mex 6.2.1, Alicona).

3. Results and discussion

3.1. Microstructural features and tensile properties

Fig. 2 shows EBSD orientation color maps of (a) pure Mg and (b) Mg–1.3Y specimens, obtained after annealing at 400 °C for 30 s and 500 °C for 60 s, respectively, following 80% hot rolling. All observations were conducted from the normal direction (ND) of the rolled sheets. Both specimens exhibited equiaxed grain morphologies with negligible intragranular orientation gradients, indicating fully recrystallized microstructures.

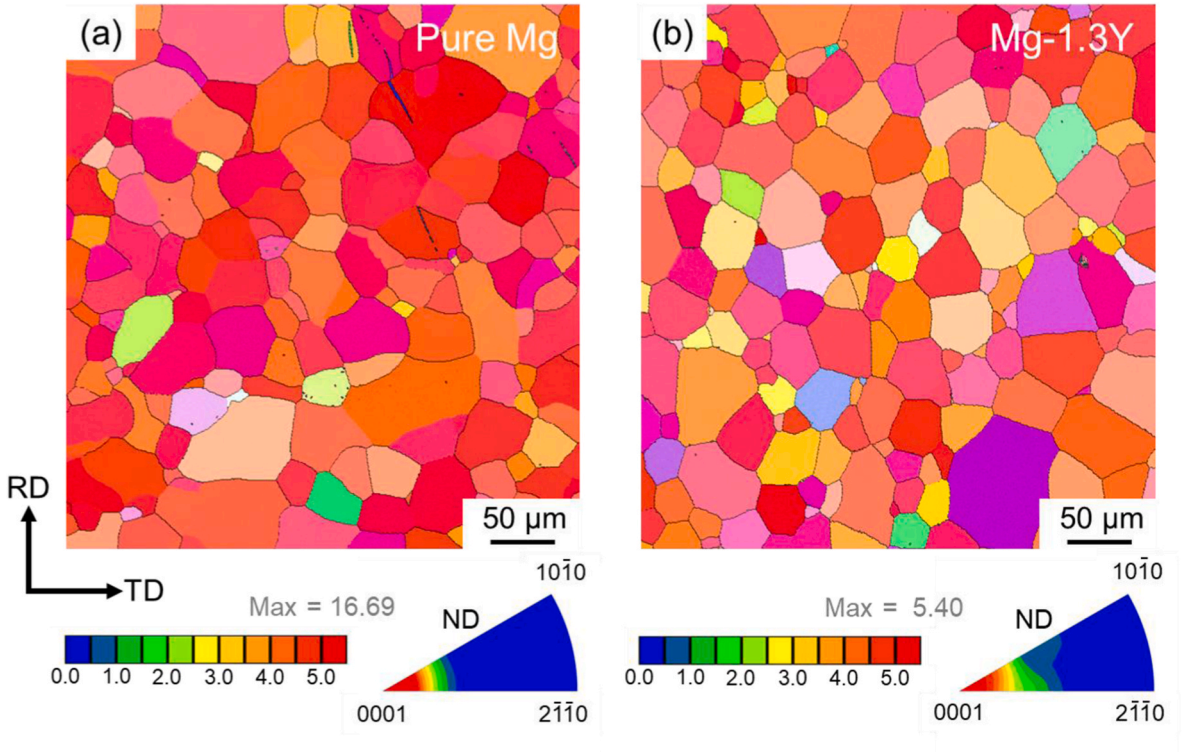


Fig. 2. EBSD orientation color maps for (a) pure Mg and (b) the Mg-1.3Y specimens, together with inverse pole figures showing the (0001) basal texture, observed from the normal direction (ND) of the sheets.

Strong (0001) basal recrystallization textures were observed in both materials, which are commonly reported for rolled and annealed Mg alloys [42–44]. The basal texture intensity was stronger in pure Mg than in Mg–1.3Y alloy, consistent with previous results [45]. A small number of deformation twins were observed in the pure Mg specimen; however, these twins are considered to have been introduced during mechanical polishing rather than during thermomechanical processing.

The average grain sizes of the pure Mg and Mg–1.3Y specimens were 25.9 μm and 22.3 μm, respectively, confirming that both materials possessed comparable grain sizes after processing. The evolution of grain size as a function of annealing condition is summarized in Fig. S1, which demonstrates that different annealing temperatures and holding times were required to achieve comparable grain sizes due to the slower grain growth in the Mg–1.3Y alloy. It should be noted that the annealing conditions employed for pure Mg and Mg–1.3Y were different, which may lead to subtle differences in the initial microstructural state, such as dislocation density, solute distribution, and grain-boundary characteristics. Therefore, the possible influence of these factors on the subsequent deformation behavior cannot be completely excluded. Nevertheless, since the primary variable in this study is grain size and comparable grain sizes were successfully achieved, the observed differences in deformation behavior are considered to be mainly governed by grain size.

Fig. 3 shows (a) nominal stress–strain curves and (b) the corresponding strain-hardening rate curves together with true stress–strain responses for pure Mg and Mg–1.3Y specimens. As shown in Fig. 3 (a), pure Mg exhibited a yield strength of 122.5 MPa and an ultimate tensile strength (UTS) of 168.5 MPa, whereas the Mg–1.3Y specimen showed a lower yield strength of 92.3 MPa and a slightly higher UTS of 173.2 MPa, respectively. A pronounced difference was observed in ductility. Notably, the Mg–1.3Y specimen exhibited a substantial improvement in ductility while maintaining a comparable stress level, consistent with previous reports on pure Mg and Mg–Y alloys [46,47]. Pure Mg exhibited limited ductility, with a uniform elongation of 0.043 and a total elongation of 0.088. In contrast, the Mg–1.3Y specimen showed significantly enhanced ductility, with a uniform elongation of 0.129 and a total elongation of 0.235. These results indicate that Y addition effectively enhances the tensile ductility of Mg while maintaining a comparable strength level.

The strain-hardening behavior also differed markedly between the two materials, as shown in Fig. 3 (b). Pure Mg exhibited a rapid decrease in strain-hardening rate with increasing strain, whereas the Mg–1.3Y specimen showed a more gradual and sustained decrease. As a result, the strain-hardening-rate curve for Mg–1.3Y intersected the true stress–-strain curve at a higher strain level. According to the Considère criterion, which defines the onset of plastic instability (macroscopic necking) as the condition where the strain-hardening rate ($d\sigma/d\varepsilon$) equals the true stress (σ), this behavior accounts for the substantially larger uniform elongation observed in the Mg–1.3Y specimen. In the following sections, detailed analyses are presented from the perspective of microstructural evolution in pure Mg and Mg–1.3Y alloys.

3.2. Evolution of deformation twinning

Fig. 4 shows the evolution of EBSD orientation maps and corresponding twin-highlighted maps obtained from identical-area observations during tensile deformation for (a) pure Mg and (b) Mg–1.3Y specimens, along with (c) the evolution of {10–12}⟨10–11⟩ tension twin fraction as a function of nominal strain up to necking. All EBSD maps were acquired from the normal direction (ND) of the sheets, and tensile deformation twins were identified and highlighted by extracting the corresponding orientations from the EBSD data. The tensile axis is aligned with the vertical direction in the images. With increasing plastic deformation, gradual intragranular orientation gradients were observed in both materials, indicating the accumulation of dislocation slip. Concurrently, the fraction of deformation tension twins increased with tensile strain (see Fig. S2). No evidence of compressive twinning was detected, which is likely due to the significantly higher critical resolved shear stress (CRSS) required for their operation [48,49] as well as large strains for their formation [50].

Because the present specimens exhibit a strong basal texture with the basal planes predominantly aligned with the ND, the activation of tension twins is crystallographically unfavorable under uniaxial tension along the rolling direction (RD). Nevertheless, a measurable fraction of tension twins was observed in both materials. This can be attributed to heterogeneous local stress states arising from grain interactions in the polycrystalline structure, which promote twin activation even under nominally uniaxial loading.

At a nominal tensile strain of 5.3%, the pure Mg specimen exhibited a twin fraction of 4.1%, whereas the Mg–1.3Y specimen reached a twin fraction of 9.4% at a higher strain of 12.3%. Notably, as shown in Fig. 4 (c), both specimens exhibited nearly identical twinning kinetics up to a tensile strain of 5.3%, as indicated by similar slopes in the twin fraction–strain curves. With further deformation, the Mg–1.3Y specimen showed a continued increase in twin fraction; however, the overall rate of increase remained comparable.

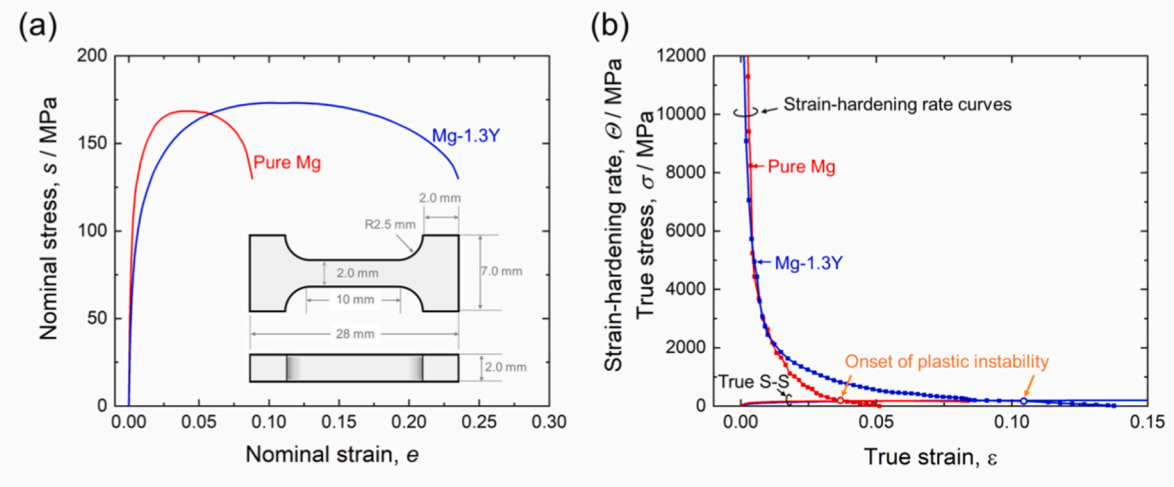


Fig. 3. (a) Nominal stress-strain curves and (b) corresponding strain-hardening rate curves with true stress-strain curves for pure Mg and Mg-1.3Y specimens. A schematic illustration of the tensile specimen geometry is included in (a). The onset of plastic instability, defined by the intersection of the strain-hardening rate curve with the true stress-strain curve, is indicated in (b).

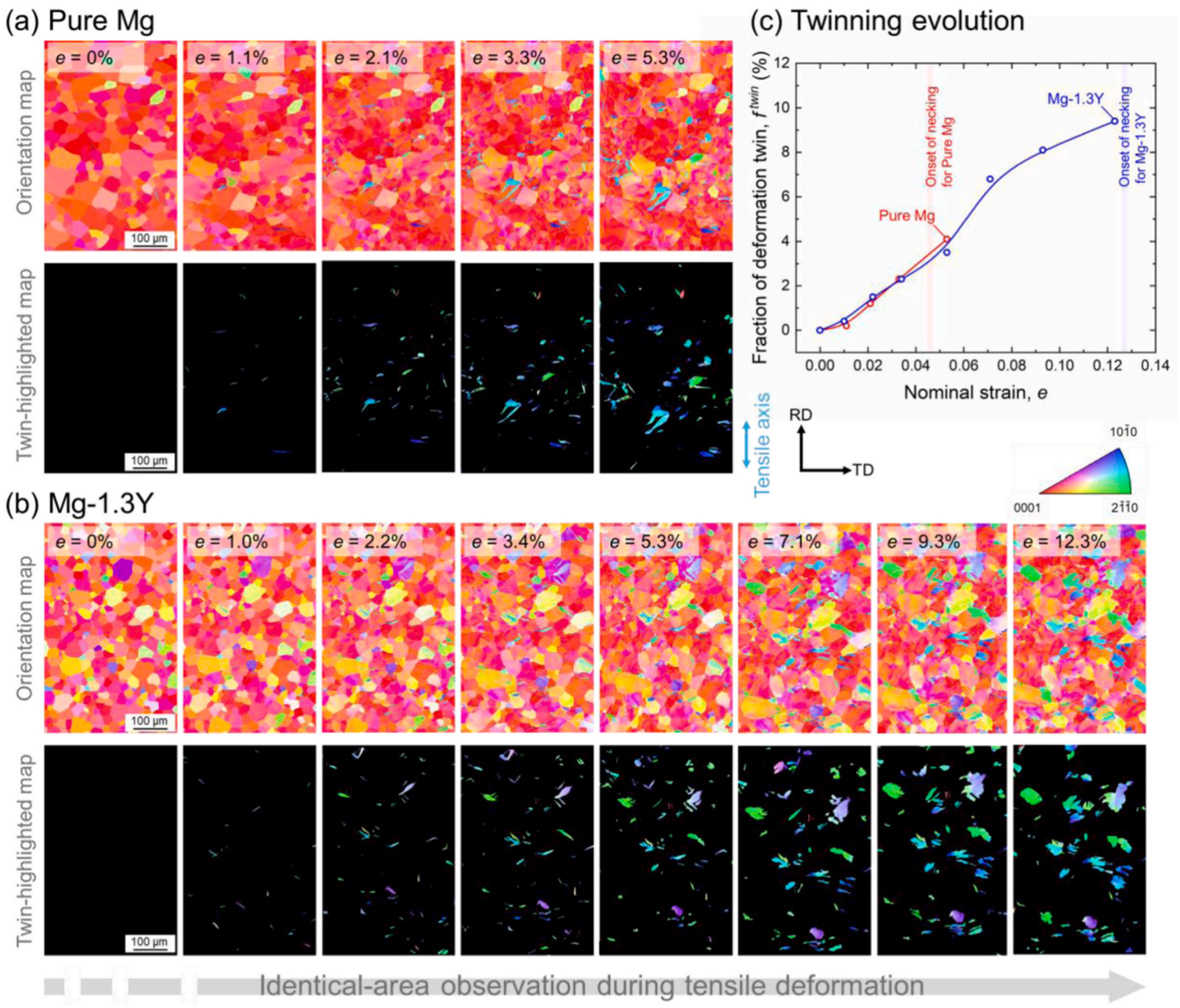


Fig. 4. Evolution of EBSD orientation color maps and {10-12} tensile deformation twin maps obtained by identical-area observations during tensile deformation for (a) pure Mg and (b) Mg-1.3Y specimens. (c) Fraction of deformation twins as a function of nominal strain.

The increase in twin fraction is primarily associated with the growth of pre-existing twins rather than extensive nucleation of new twins. Such twin growth provides additional ⟨c+a⟩ shear accommodation in the HCP crystal structure and may contribute, at least in part, to the enhanced ductility of the Mg–1.3Y specimen.

3.3. Activation of dislocation slip

In this section, the differences in tensile behavior between pure Mg and Mg–1.3Y specimens are examined from the perspective of dislocation slip activation. Slip lines formed during deformation were carefully observed using SEM. Owing to the strong basal texture, basal slip lines could not be clearly identified from the normal direction (ND) of the tensile specimens. Therefore, the transverse direction (TD) plane was manually polished to enable direct observation of slip traces associated with basal slip activation.

To assist slip-system identification, EBSD analysis was performed in the unloaded state to obtain the crystallographic orientations of individual grains, which were used as a reference for subsequent slip-line analysis of basal, prismatic, and pyramidal slip systems. Fig. 5 (a) presents a representative example of slip-line analysis in the Mg–1.3Y specimen after tensile deformation to 6.6%, together with a schematic illustration of the observation plane. Fig. 5 (b) shows slip-activation maps in which individual grains are colored according to the activated slip systems for pure Mg deformed to 6.0% strain and Mg–1.3Y deformed to 6.6% strain. In total, 77 grains in pure Mg and 76 grains in Mg–1.3Y were analyzed. While this number of grains provides a reasonable statistical basis for identifying overall tendencies in slip activity at the mesoscopic scale, it should be noted that the analysis is limited to a single deformation state and may not fully capture all possible deformation behaviors.

Deformation twinning in Mg alloys is generally promoted with increasing grain size; however, since both materials in this study have comparable grain sizes (~25 μm), the influence of grain size on twinning activity is expected to be similar in both specimens and does not affect the comparative discussion in this study.

In both specimens, single basal ⟨a⟩ slip was the predominant deformation mode, accompanied by a small fraction of grains exhibiting single non-basal slips. Multiple-slip activity was also observed; however, only 5 grains exhibited multiple slip in pure Mg, whereas 13 grains were

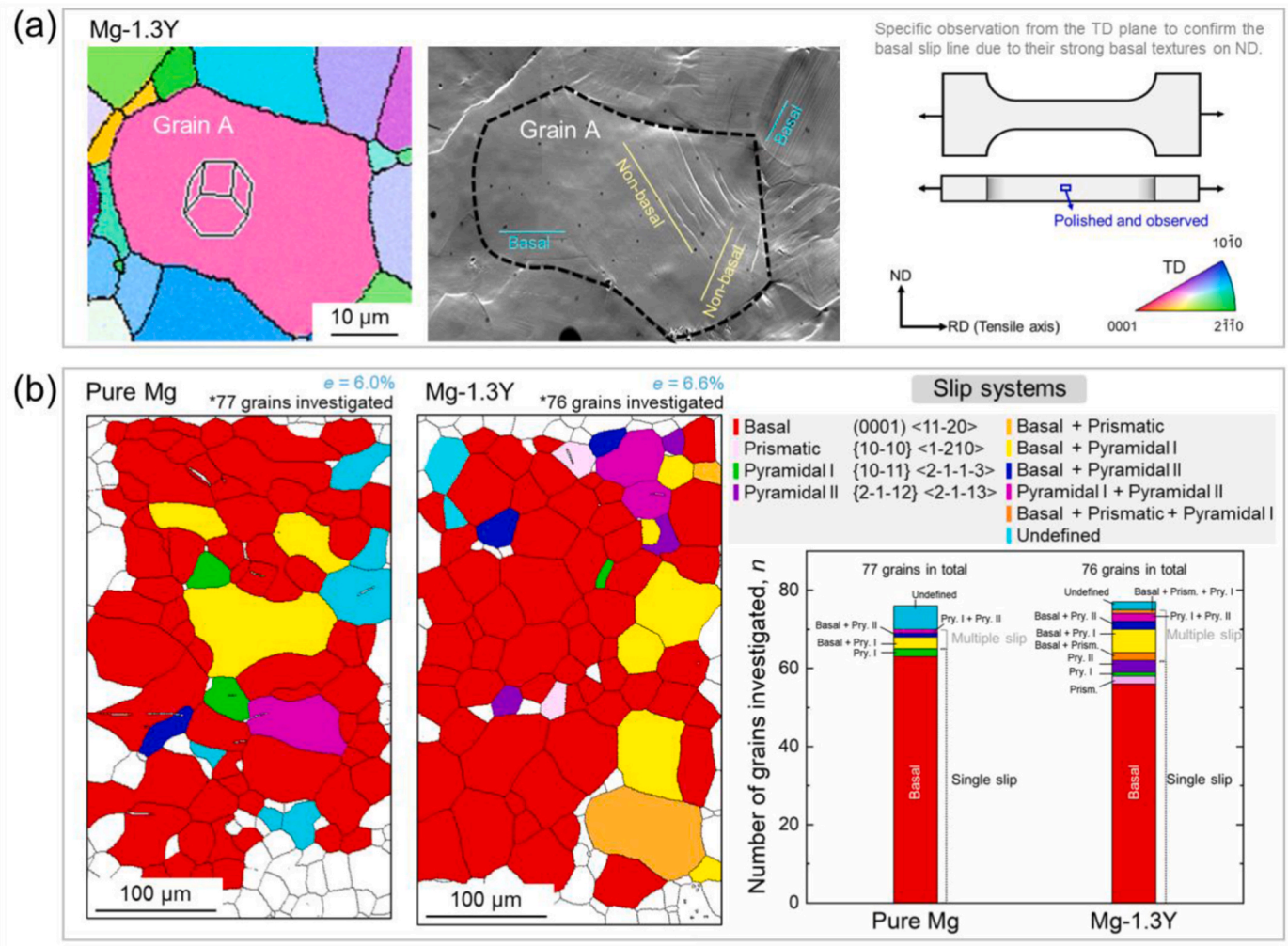


Fig. 5. (a) Representative SEM image showing slip-line analysis combined with crystallographic orientation information obtained by EBSD analysis. (b) Slip-activation maps of pure Mg and Mg-1.3Y specimens derived from SEM-based slip-line analysis. For statistical reliability, 77 grains for pure Mg and 76 grains for Mg-1.3Y were analyzed. The bar chart summarizes the fraction of each activated slip system.

identified in the Mg–1.3Y specimen. These results indicate that, at the mesoscopic scale examined in this study, plastic deformation in both materials is dominated by basal slip. These results indicate that, within the investigated conditions, plastic deformation in both materials is predominantly governed by basal slip at the mesoscopic scale.

At first glance, this observation appears inconsistent with previous reports suggesting that Y addition promotes the activation of non-basal ⟨c+a⟩ slip systems in Mg alloys [51–53]. However, this apparent difference primarily arises from the substantially different length scales probed by the experimental techniques. The present study focuses on mesoscopic-scale SEM observations to capture deformation behavior directly relevant to macroscopic mechanical response. In contrast, ⟨c+a⟩ slip activity reported in the literature has mainly been identified by TEM, which probes dislocation activity at the nanometer scale. As a result, highly localized ⟨c+a⟩ slip occurring near grain boundaries, although potentially important for strain accommodation, is unlikely to be directly resolved at the SEM scale. Therefore, the absence of extensive non-basal slip features in the present SEM observations does not contradict previous TEM-based findings.

From this perspective, macroscopic ductility should be interpreted primarily in terms of mesoscopic deformation behavior, rather than solely on the basis of microscopic TEM observations or atomistic-scale simulations [15,47]. While the activation of non-basal ⟨c+a⟩ slip may contribute to ductility enhancement induced by Y addition, the present results suggest that it is not the dominant mechanism under the investigated conditions.

With respect to strain compatibility, deformation accommodated exclusively by basal slip inevitably leads to displacement discontinuities at grain boundaries, which are expected to play a critical role in limiting ductility. This issue is examined in the next section from the viewpoints of local strain distribution and surface depth evolution.

3.4. Local strain distributions and grain boundary discontinuity

Fig. 6 shows the evolution of SEM microstructures during tensile deformation and the corresponding DIC strain distribution maps for (a) pure Mg and (b) Mg–1.3Y specimens. All observations were conducted from the normal direction (ND) of the tensile specimens, with the tensile axis oriented horizontally in the images. It should be noted that the fine contrast observed in the SEM images is mainly attributed to colloidal silica (SiO_2) particles used as speckle pattern for DIC analysis, and does not correspond to second-phase particles (see Fig. S3). In the DIC maps, the color scale represents the normal strain component along the tensile axis (ε_{11}), as indicated by the color bar. Both specimens were tensile-deformed to approximately 4%.

Clear microstructural evolution was observed in both materials during deformation. Interestingly, in pure Mg, pronounced surface steps, likely originating at grain boundaries, appeared at an early stage of deformation and became increasingly prominent with further straining. Such a surface step at the grain boundary was also observed in

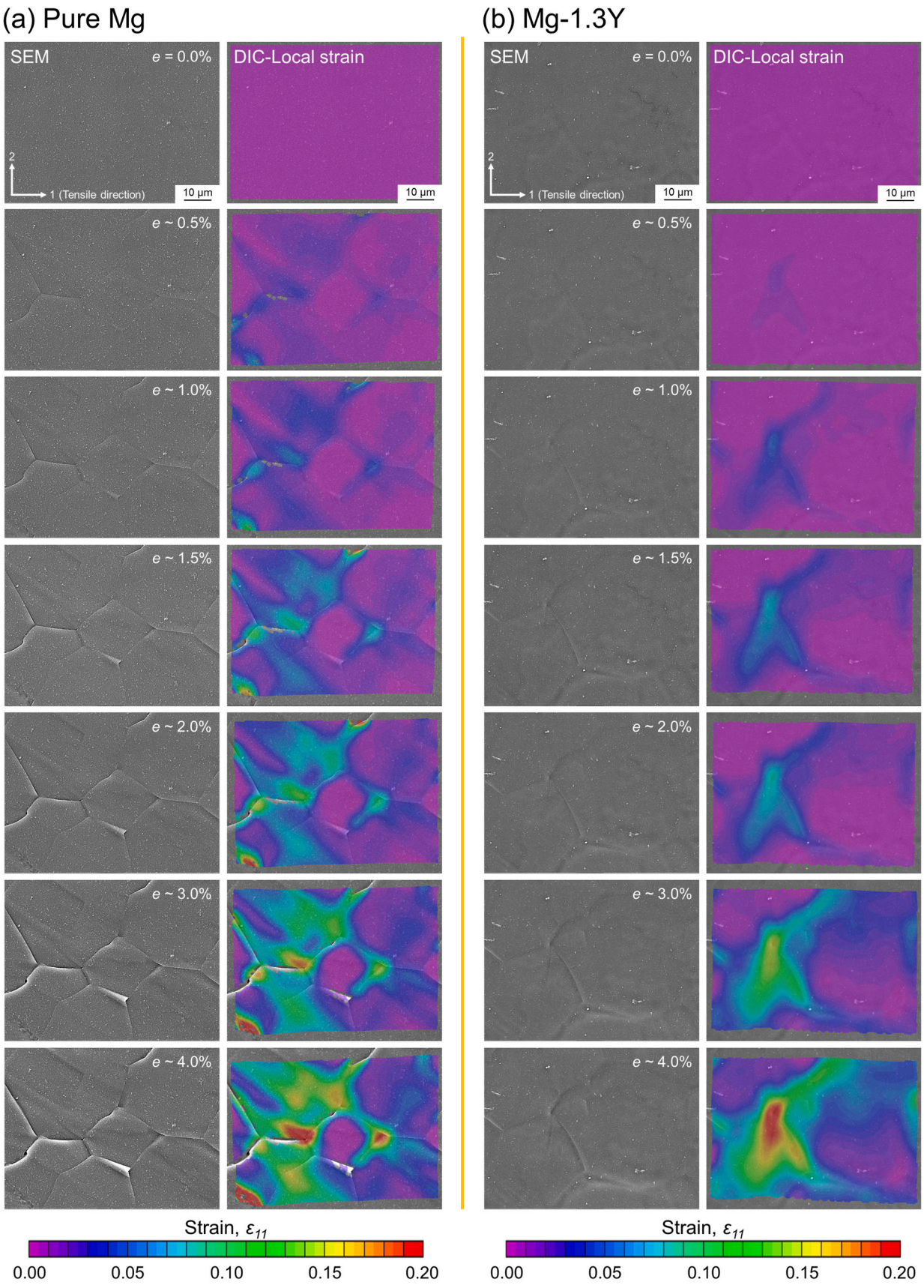


Fig. 6. Evolution of local deformation and the corresponding strain distribution maps obtained by digital image correlation (DIC) during tensile deformation of (a) pure Mg and (b) Mg-1.3Y specimens. The tensile axis is oriented horizontally in the images, and the color scale in the DIC maps represents the normal strain component along the tensile direction.

the Mg–1.3Y specimen, but the magnitude the surface steps was considerably smaller than that in pure Mg. In contrast, although surface steps at grain boundaries were also observed in the Mg–1.3Y specimen, their magnitude was considerably smaller than that observed in pure Mg. These results indicate a difference in displacement continuity at grain boundaries, which is likely related to heterogeneous deformation.

The DIC strain maps revealed highly heterogeneous local strain distributions in both specimens. Interestingly, strain localization occurred on a grain-by-grain basis, such that some grains experienced intense deformation, whereas others remained nearly undeformed. These observations indicate that surface steps at grain boundaries are closely related to strong strain partitioning between neighboring grains.

A statistical analysis of deformation heterogeneity was performed, and the results are presented in Fig. 7 (a). Grain-averaged strain exhibits a bimodal distribution in both specimens, indicating pronounced heterogeneity. However, the nature of strain localization differs. In pure Mg, a limited number of grains exhibit exceptionally high strain, indicating strong and localized strain concentration. In contrast, the Mg–1.3Y alloy shows a broader distribution of moderately strained grains with fewer extreme values. This difference indicates that strain localization in pure Mg is more severe and spatially concentrated, whereas in the Mg–1.3Y alloy, strain is more widely distributed among multiple grains, reducing the likelihood of deformation discontinuity at grain boundaries.

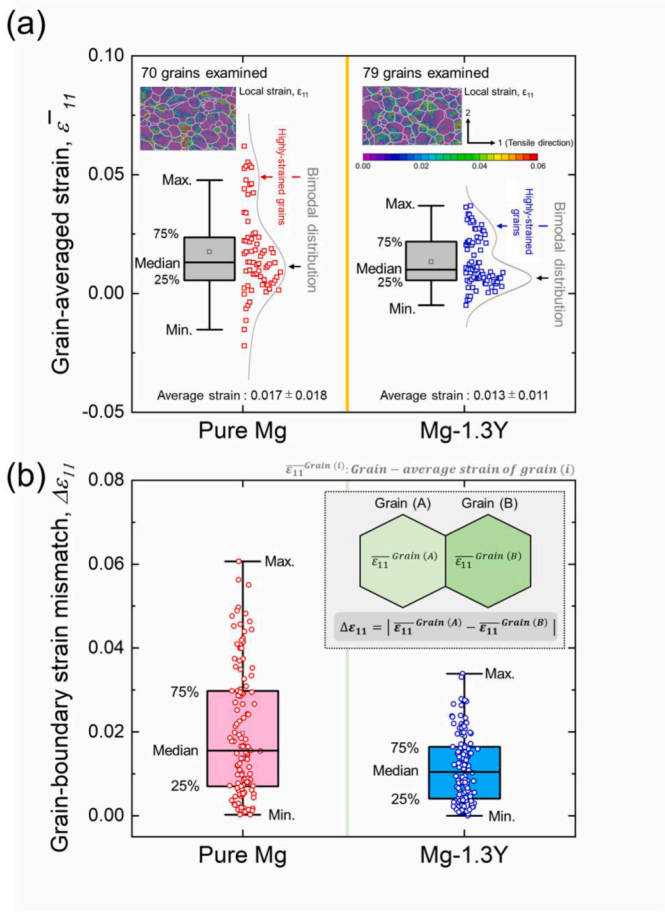


Fig. 7. (a) Statistical comparison of grain-averaged strain (ε_{11}) in pure Mg and Mg–1.3Y specimens at a similar macroscopic strain level (~2%). Box plots represent the interquartile range (25–75%) with median values, while whiskers indicate the minimum and maximum values. Individual grain data are overlaid as scatter points, and the corresponding distributions are shown as density plots. Insets show the local strain maps analyzed for the statistical evaluation, obtained by μ-DIC. (b) Grain-boundary strain mismatch ($\Delta\varepsilon_{11}$) in pure Mg and Mg–1.3Y specimens, calculated from the grain-averaged strain data shown in (a). The inset schematically illustrates the definition of grain-boundary strain mismatch as the absolute strain difference between neighboring grains.

Fig. 7 (b) shows the statistical distribution of grain-boundary strain mismatch ($\Delta\varepsilon_{11}$), defined as the difference in grain-averaged strain between neighboring grains. Pure Mg exhibits a broader distribution with higher maximum values, whereas the Mg–1.3Y alloy shows a narrower distribution with lower median and maximum values. These results demonstrate that grain-boundary strain mismatch is significantly suppressed in the Mg–1.3Y alloy, indicating improved strain compatibility and contributing to enhanced ductility. Overall, these results suggest that the enhanced ductility of the Mg–1.3Y alloy can be attributed, at least in part, to the suppression of strain incompatibility at grain boundaries, enabled by more distributed deformation among grains.

Fig. 8 presents a representative example of the pure Mg specimen exhibiting severe cracking at a grain boundary, together with the corresponding DIC strain distribution maps during tensile deformation to approximately 4%. Enlarged SEM images of the same region are also provided. At a tensile strain of 1.0%, a clear deformation discontinuity was observed at the grain boundary, across which pronounced strain partitioning was recognized. Only the central grain (located at the center of the DIC strain distribution maps) accommodated a large strain, whereas the surrounding grains exhibited minimal deformation. These observations indicate that the deformation discontinuity at the grain boundary is associated with the highly heterogeneous nature of grain-scale deformation.

With further deformation to a tensile strain of 2%, the displacement discontinuity became more pronounced and developed into a microcrack. At this stage, the microcrack exhibited a length of approximately 16 μm and a width of about 4 μm. The surrounding grains exhibited little plastic deformation, while strain localized in the central grain tended to propagate preferentially along grain boundaries. Upon further deformation to a tensile strain of 4%, the microcrack grew significantly, reaching a length of 21 μm and a width of 10.2 μm. This microcrack is expected to act as a strong stress concentration site, potentially promoting early tensile failure. Notably, the initiation and propagation of a relatively large microcrack occurred within the uniform elongation regime, indicating that severe local damage can develop even during macroscopically stable deformation.

Since Fig. 8 presents an extreme example of microcrack formation in pure Mg, the overall tendency for deformation discontinuity at grain boundaries was further examined in Fig. 9. Considering that deformation discontinuities appear as sharp edge contrast in SEM images, edge-highlighted maps were constructed using image-processing software (ImageJ 1.54d, National Institutes of Health, Bethesda, MD, USA).

Overall view of Grain-boundary surface steps was qualitatively evaluated by detecting pronounced contrast variations that developed along grain boundaries during deformation. Edge-highlighted images were generated to emphasize these contrast changes, with the intensity represented in blue, thereby enabling the identification of microcrack-like features and/or surface step formation associated with deformation. In these images, edge contrast is shown in blue, while regions corresponding to microcrack-like features identified from SEM observations are highlighted in orange.

Fig. 9 (a) shows the procedure used to generate the edge-highlighted image, using a representative example from the pure Mg specimen. Fig. 9 (b) presents the evolution of SEM images and the corresponding edge-highlighted images for the pure Mg specimen at nominal strains of approximately 2% and 4%. Even at a relatively low strain of about 2%, localized edge contrast (blue) intensification is already observed along several grain boundaries, indicating the early development of deformation-induced surface steps. Notably, microcrack-like features (orange) are already observed at some grain boundaries. With further deformation to about 4%, the number of such microcrack-like features increases markedly.

In contrast, Fig. 9 (c) shows the corresponding results for the

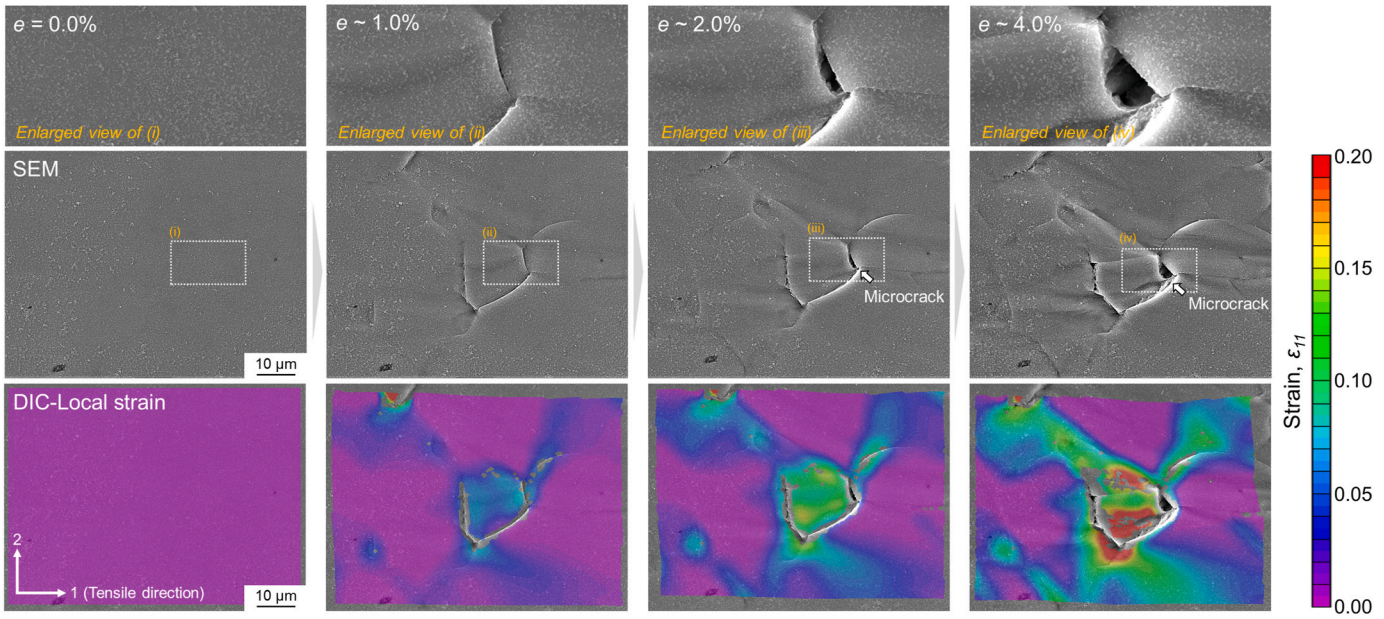


Fig. 8. SEM microstructures and corresponding DIC strain distribution maps obtained during tensile deformation in the pure Mg specimen. An enlarged view highlights the region exhibiting severe microcrack formation.

Mg–1.3Y specimen. Several isolated blue contrasts with globular shapes are considered to originate from minor surface artifacts, such as contamination, rather than deformation-induced grain-boundary steps. Although some grain boundaries exhibit moderate contrast changes, their intensity is clearly weaker than that in pure Mg, even at a strain of approximately 4%. No clear microcrack-like features are observed along grain boundaries even at this strain level.

Despite the semi-quantitative nature of this image-based edge-detection analysis, these results clearly indicate that, although deformation-induced grain-boundary steps are present in both materials, clear microcrack-like features are observed only in pure Mg within the present observations, whereas no such features are identified in the Mg–1.3Y alloy. This observation is consistent with the statistical strain analysis shown in Fig. 7, which indicates more localized strain distribution in pure Mg. Therefore, the improved strain compatibility in the Mg–1.3Y alloy is considered to contribute to enhanced ductility by suppressing strain localization and deformation heterogeneity.

To further characterize surface deformation, depth variations along the normal direction (ND) of the pure Mg specimen were examined using a three-dimensional (3D) surface measurement technique. Fig. 10 shows the procedure for 3D surface reconstruction and the reconstructed 3D surface topography together with a quantitative depth profile for (a) pure Mg and (b) Mg-1.3Y specimens tensile-deformed to approximately 4%. The 3D surface topology was reconstructed using three SEM images acquired from an identical area at tilt angles of -5°, 0°, and $+5^{\circ}$ relative to the incident electron beam.

In pure Mg, pronounced depth steps were clearly observed at grain boundaries in the reconstructed depth color map. The 3D surface topography reveals significant depth variations associated with grain boundaries. The depth profile measured along an inspection line across the boundary between Grain I and Grain II exhibits a sharp change in surface height at the grain boundary.

In contrast, the Mg–1.3Y specimen shows much smoother surface variations with significantly reduced depth steps at grain boundaries. The corresponding depth profile reveals a more gradual change in surface height across the grain boundary. These results provide direct three-dimensional evidence that grain-boundary surface steps are significantly reduced in the Mg–1.3Y alloy, consistent with the statistical edge-highlighting analysis presented in Fig. 9.

Since the depth profiles shown above were obtained from representative grain boundaries exhibiting relatively pronounced surface steps, a statistical analysis of surface step height was further conducted to assess the overall trend across the microstructure, as summarized in Fig. 11. The results clearly show that the Mg–1.3Y specimen exhibits significantly lower surface step heights compared to pure Mg, confirming that grain-boundary surface steps are systematically reduced in the Mg–1.3Y alloy.

Such pronounced depth steps at grain boundaries in pure Mg can be associated with the limited availability of active slip systems in the HCP structure. Although non-basal slip activity was limited at the SEM mesoscopic scale in both specimens (Fig. 5), previous studies have reported that non-basal slip can be locally activated near grain boundaries in Mg–Y alloys. While such localized activity cannot be directly resolved in the present analysis, it may contribute to alleviating surface step formation at grain boundaries. Therefore, the observed difference in grain-boundary surface steps between pure Mg and Mg–1.3Y is considered to reflect differences in local strain accommodation behavior manifested at the SEM scale.

Fig. 12 presents schematic illustrations of two neighboring grains showing the formation of a surface step, viewed from the transverse direction (TD), before and during tensile deformation. In this schematic, only the activation of the (0001) basal slip system is considered. Grain A is assumed to be an easily deformable grain, characterized by a tilting angle θ that deviates from 90° between the c-axis of the HCP crystal and the tensile direction, whereas Grain B is assumed to be a plastically hard grain with a tilting angle close to $\theta \approx 90^{\circ}$. In this situation, θ can also be interpreted as the relative difference in c-axis orientation between Grain A and Grain B with respect to the tensile axis. This assumption is reasonable because both specimens exhibit strong (0001) basal textures with small angular deviations in some grains.

For simplicity, deformation is treated as two-dimensional, and the $\langle 11\text{–}20 \rangle$ slip direction is assumed to lie in the in-plane direction. Under applied tensile stress, Grain A can activate (0001) basal slip, resulting in simple shear deformation characterized by a simple shear strain $\gamma = b/d$, where b denotes the slip displacement and d represents the thickness of the deforming element. Such preferential slip activity in Grain A is expected to induce the formation of a depth step at the grain boundary.

The resulting depth step, h, can be interpreted as a displacement component (u_2) along the normal direction (ND) in the global coordinate system. Accordingly, the simple shear deformation and the

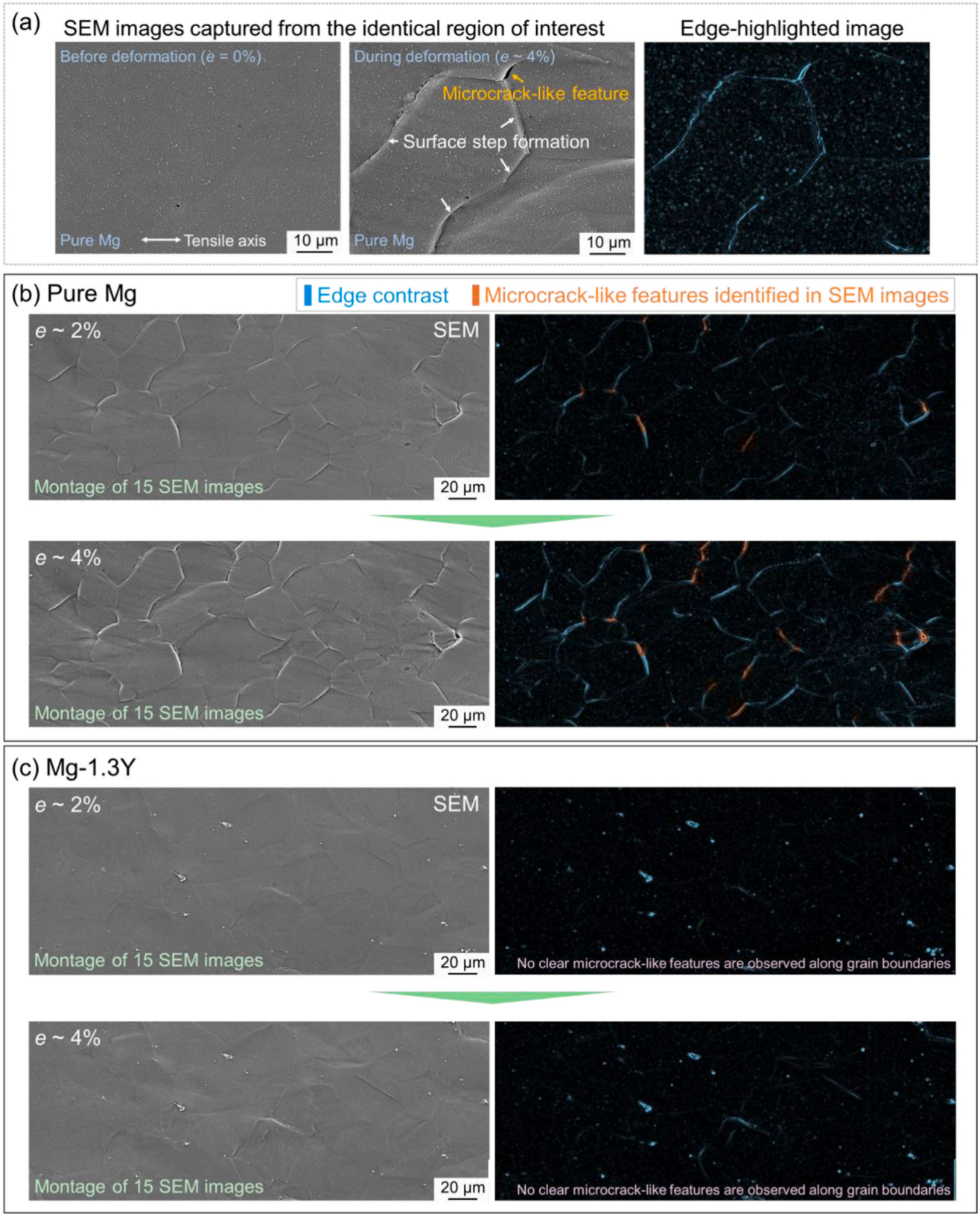


Fig. 9. Wide-area SEM observations and corresponding edge-highlighted images showing the evolution of grain-boundary surface features in pure Mg and Mg–1.3Y alloys during tensile deformation. (a) Representative SEM images of an identical area in pure Mg before deformation ($e = 0\%$) and during deformation ($e \sim 4\%$), illustrating the development of grain-boundary surface steps accompanied by microcrack-like features. (b, c) Wide-area SEM microstructures (montage of 15 SEM images) and corresponding edge-highlighted images for (b) pure Mg and (c) Mg–1.3Y specimens at tensile strains of approximately 2% and 4%. In the edge-highlighted images, edge contrast is shown in blue, while regions corresponding to microcrack-like features identified from SEM observations are highlighted in orange.

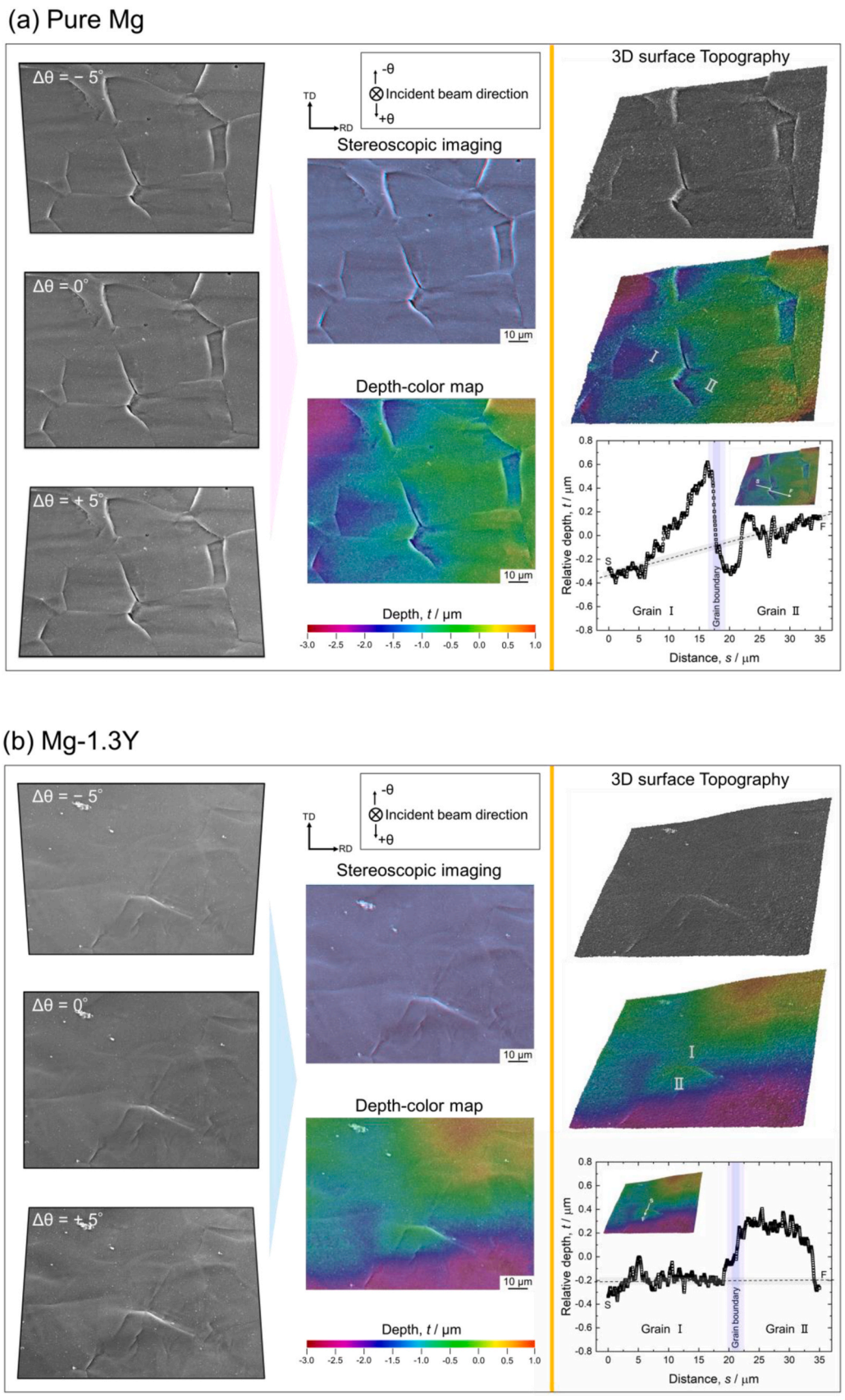


Fig. 10. Three-dimensional (3D) SEM topography and depth profiling revealing grain-boundary surface steps in (a) pure Mg and (b) Mg–1.3Y specimens tensile-deformed to ~4% strain. For each material, the left panels show SEM images acquired at different tilt angles ($\Delta\theta = -5°$, 0°, +5°) used for 3D reconstruction. The middle panels present the reconstructed surface morphology, and the right panels show the corresponding 3D surface topography and depth profiles across representative grain boundaries.

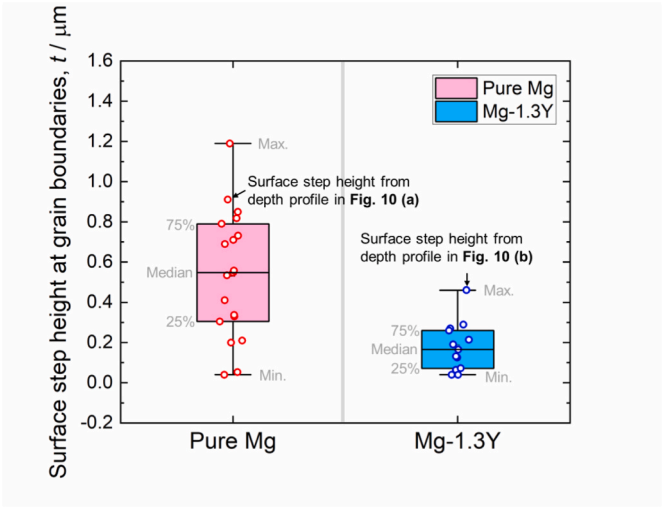


Fig. 11. Statistical comparison of grain-boundary surface step height in pure Mg and Mg–1.3Y specimens. Box plots represent the interquartile range (25–75%) with median values, while whiskers indicate the minimum and maximum values. Individual data points are overlaid.

associated displacement components (u_i) occurring in Grain A, initially described in the local coordinate system defined by the (0001) basal plane normal and slip direction, must be transformed into the global coordinate system to quantify the depth step. Under these assumptions, the displacement component ($u_2 = h^{local}$) along ND within the deformation element can be simply expressed as $\gamma d \sin\theta$.

Further assuming that Grain An undergoes uniform deformation in its interior with a shear strain γ, the macroscopic depth step observed experimentally can be expressed as $\gamma d_1 \sin\theta$, where d_1 denotes the grain size of Grain A measured along the c-axis direction. Although this relationship is derived under simplified assumptions—namely, single-slip activation in the in-plane direction and approximately uniform intragranular deformation—it clearly indicates that the magnitude of the surface step is governed by the shear strain γ, the relative orientation angle θ between neighboring grains (or with respect to the global ND), and notably, the grain size d_1.

While this schematic description is primarily constructed for the pure Mg specimen, it also provides a useful framework for understanding the enhanced ductility of the Mg–1.3Y specimen. In Mg–1.3Y, surface steps at grain boundaries are expected to be more effectively accommodated through the activation of additional slip systems. As observed in Fig. 6 (b) and Fig. 9 (c), although contrast variations along grain boundaries are present in the Mg–1.3Y specimen, sharp surface steps comparable to those in pure Mg are not clearly developed. This suggests enhanced strain accommodation at grain boundaries, plausibly associated with the activation of multiple slip systems, including non-basal ⟨c+a⟩ slips, which have been confirmed by several research groups through TEM observations [9,11,13,15,51].

More generally, in FCC and BCC materials, where multiple independent slip systems are readily activated, strain incompatibilities at grain boundaries can be more efficiently relaxed. This suppresses the formation of pronounced surface steps and contributes to improved overall ductility.

In addition to slip activity, grain-boundary shear or sliding has frequently been reported in Mg and Mg-based alloys [54–56]. Hauser et al. [57] reported grain-boundary sliding in coarse-grained Mg through the observation of discontinuities in surface grid lines at grain boundaries. Zheng et al. [58] further demonstrated that grain-boundary sliding becomes a predominant deformation mode in ultrafine-grained pure Mg with a grain size of approximately 0.65 μm. These previous studies suggest that Mg-based materials may exhibit relatively low resistance to grain-boundary deformation compared to other structural metallic materials.

The addition of Y is also expected to modify grain-boundary characteristics, particularly grain-boundary energy. Barrett et al. [59] calculated grain-boundary energy and mobility in Mg with Y segregation

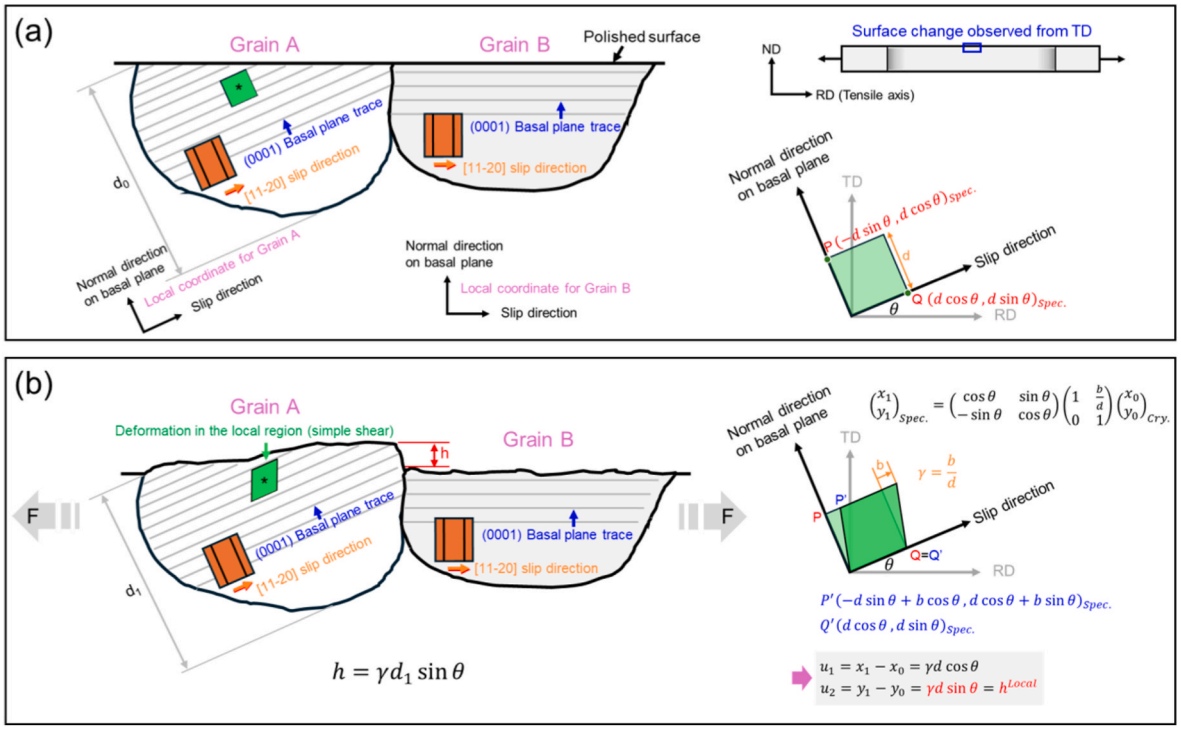


Fig. 12. Schematic illustrations of surface-step formation observed from the transverse direction (TD), considering single (0001) basal slip: (a) before and (b) during tensile deformation. Grain A is assumed to be an easily deformable grain with a high Schmid factor, whereas Grain B is assumed to be a plastically hard grain with a low Schmid factor.

and reported that Y segregation at grain boundaries is energetically more stable than in pure Mg, except for special high-symmetry grain boundaries such as coincidence site lattice (CSL) boundaries. Although the mechanical resistance of Y-segregated grain boundaries against externally applied deformation remains quantitatively unclear, such segregation effects may influence the mechanical stability of grain boundaries by alleviating strain and deformation discontinuities across grain boundaries. In this context, the role of Y segregation can be considered as a possible contributing factor based on previous studies. Such an effect is consistent with the reduced grain-boundary deformation discontinuity and suppressed microcrack formation observed in the Mg–1.3Y alloy, which indicate improved strain compatibility at grain boundaries. However, direct experimental evidence for this effect is not provided in the present study, and further investigation using advanced characterization techniques, such as TEM or atom probe tomography, will be required to directly verify solute segregation at grain boundaries and its mechanical implications.

It should also be noted that the possible presence of nanoscale precipitates cannot be excluded. In Mg–Y alloys, nano-sized $Mg_{24}Y_5$ precipitates have been reported to form during prolonged annealing [60–62], which may also influence the mechanical response. Although such effects are beyond the scope of the present study, they warrant further investigation in future work.

3.5. Comprehensive understanding of ductility enhancement in Mg–Y alloy

So far, the ductility enhancement observed in the Mg–1.3Y specimen has been systematically investigated through comparison with pure Mg from multiple perspectives, including deformation twinning behavior, slip activity, deformation heterogeneity, and the development of discontinuities at grain boundaries. In particular, the significance of grain-boundary discontinuities in governing mechanical properties has been emphasized throughout this study. In this final section, an integrated view combining SEM microstructural observations, DIC-based deformation heterogeneity analysis, and EBSD-derived Schmid factor maps is presented to provide a comprehensive understanding of how microstructural deformation behavior governs the macroscopic tensile properties of the Mg–Y alloy.

Fig. 13 shows identical-area characterization using SEM, DIC, and EBSD analyses for (a) pure Mg and (b) Mg-1.3Y specimens tensile-deformed to approximately 2%. For each condition, forty SEM images were captured and merged to construct a single montaged image. DIC strain analysis was performed on each individual SEM image, and the resulting strain maps were subsequently merged to obtain the corresponding large-area strain distribution. Grain boundary was indicated by white lines on strain distribution maps, and the color scale represents the normal strain component along the tensile axis (horizontal direction), ε_{11}. EBSD-derived Schmid factor maps for basal slip, showing the maximum Schmid factor value, were obtained in the undeformed condition ($e = 0\%$). From the SEM montage, the two specimens were found to exhibit markedly different behaviors with respect to intergranular discontinuities. In the pure Mg specimen, intergranular discontinuities appeared much sharper and more pronounced than those observed in the Mg–1.3Y specimen. Nevertheless, it should be emphasized that distinct grain-boundary contrast is still clearly present in the Mg–1.3Y specimen, albeit with a reduced magnitude compared to pure Mg. Such grain-boundary-associated surface contrast, which can still be identified in the Mg–1.3Y alloy, is a characteristic feature of HCP Mg alloys and is rarely observed in FCC or BCC materials, where strain incompatibilities are more efficiently accommodated by multiple independent slip systems.

DIC strain distribution maps revealed highly heterogeneous deformation in both specimens. Specifically, the local strain distribution could be broadly categorized into two characteristic groups: (i) grains exhibiting very low strain levels (typically below ~0.5%), appearing in purple, and (ii) grains accommodating relatively high strain, represented by green to red colors.

Selected views highlighting grains with high Schmid factors (>0.24) are provided below the full-field DIC strain distribution and EBSD-based Schmid factor maps to clarify the relationship between Schmid factor and local strain in polycrystalline pure Mg and Mg–1.3Y specimens. Grains exhibiting pronounced strain localization tend to show relatively high Schmid factors in both materials. This observation is consistent with the general expectation that grains with higher Schmid factors can more readily activate slip under a given applied stress. However, this tendency alone cannot fully explain the observed strain distribution, as a substantial fraction of grains does not strictly follow this correlation. In particular, neighboring grains adjacent to highly strained grains often exhibit noticeable deformation despite having relatively low Schmid factors, as indicated by the black arrows.

Two possible reasons can be considered for the occurrence of highly strained regions in grains with low Schmid factors. First, in polycrystalline materials, the local stress state is not purely uniaxial with only a σ_{11} component, but rather a complex multiaxial stress condition arising from mechanical interactions among neighboring grains. Consequently, the deformation behavior of individual grains cannot be described solely by the Schmid factor evaluated under an ideal uniaxial stress assumption. Second, both specimens exhibit the formation of strain-localized bands, suggesting that intense deformation in grains with high Schmid factors tends to propagate into adjacent grains, even when those neighboring grains possess relatively low Schmid factors. Such deformation transfer is likely driven by the need to relax strong strain partitioning and maintain strain compatibility. To plastically deform these less favorably oriented neighboring grains, substantially higher internal stresses are required, which can lead to local stress concentration within the strain-localized bands.

It should be noted that no substantial differences in grain-scale deformation heterogeneity were observed between the pure Mg and Mg–1.3Y specimens. Although Mg–Y alloys have been widely reported to facilitate the activation of non-basal ⟨c+a⟩ slip systems, which is generally expected to promote more homogeneous plastic deformation, such homogenization was not clearly observed in the Mg–1.3Y specimen in the present study. Instead, pronounced deformation heterogeneity persisted, similar to that in pure Mg.

This observation strongly suggests that basal ⟨a⟩ slip remains the dominant deformation mode in the Mg–1.3Y specimen, leading to strong plastic anisotropy at the mesoscopic scale, as evidenced by the slip-activation analysis in Fig. 5. Accordingly, the activation of non-basal ⟨c+a⟩ slip is likely to be spatially limited, occurring preferentially in specific regions such as near grain boundaries rather than uniformly throughout the grains.

Although enhanced activation of non-basal ⟨c+a⟩ slip in Mg–Y alloys has been widely reported in previous studies, particularly based on TEM-scale observations, the present SEM-based slip-trace analysis indicates that basal slip remains the dominant deformation mode at the mesoscopic scale. No clear increase in non-basal slip activity was observed in the Mg–1.3Y alloy compared with pure Mg within the resolution of the present analysis.

In contrast, a marked reduction in grain-boundary surface steps and strain discontinuity was clearly identified in the Mg–1.3Y alloy. The statistical analysis of grain-boundary strain mismatch further confirms that strain incompatibility across grain boundaries is significantly suppressed. These results suggest that the enhanced ductility of the Mg–1.3Y alloy is primarily governed by improved grain-boundary strain compatibility, rather than by a direct increase in non-basal slip activity at the mesoscopic scale.

It should be noted that non-basal slip may still be locally activated at a finer scale, particularly in the vicinity of grain boundaries, and could contribute to the relaxation of strain incompatibility. However, such localized activity cannot be directly resolved within the spatial resolution of the present SEM-based analysis and therefore remains

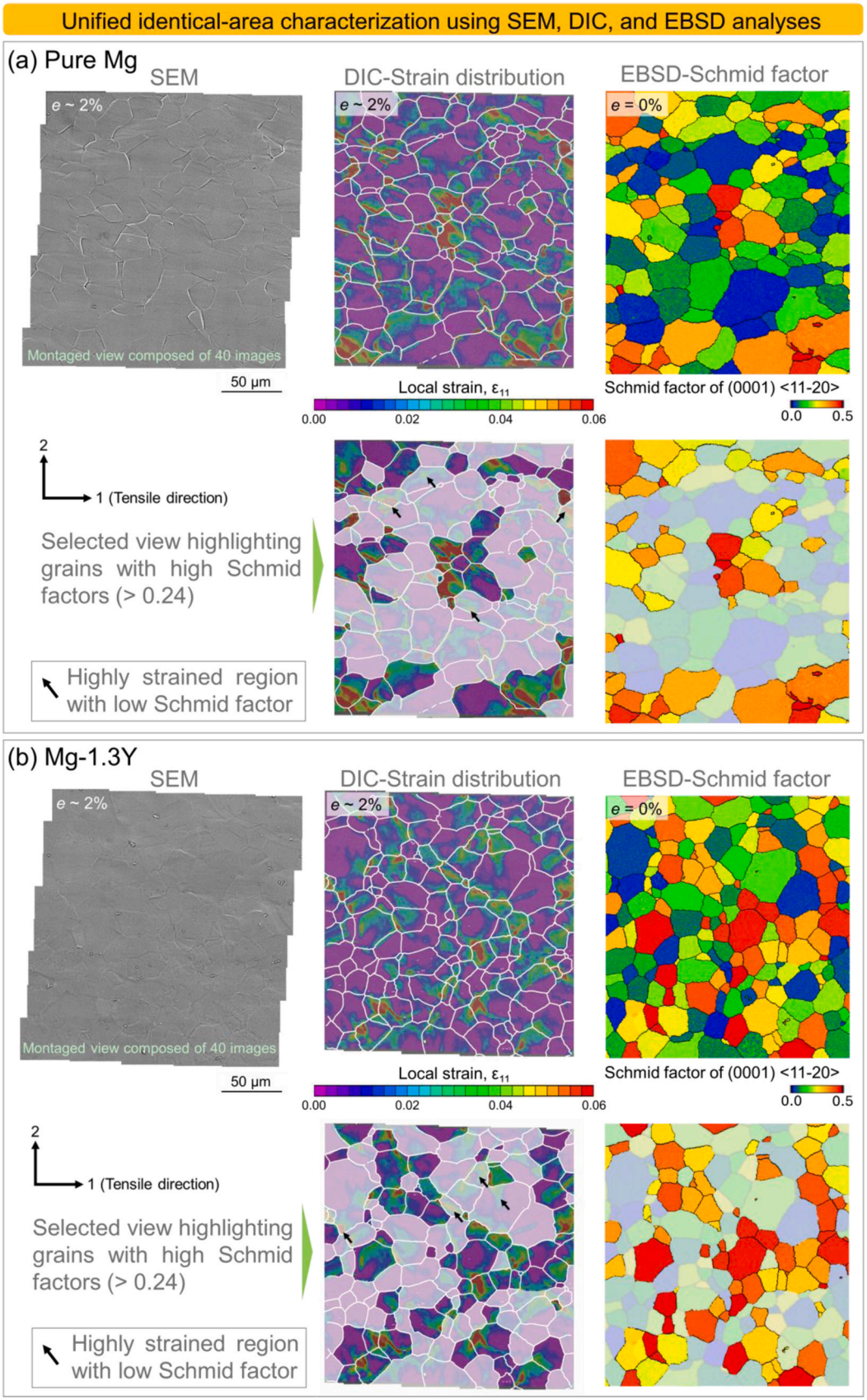


Fig. 13. Montaged views composed of forty SEM images, together with the corresponding local strain distribution and Schmid factor maps for (a) pure Mg and (b) Mg-1.3Y specimens, obtained by unified characterization of the identical area using SEM, DIC, and EBSD analyses. Selected views highlighting grains with high Schmid factors (>0.24) are shown below the full-field DIC strain distribution and EBSD-based Schmid factor maps to clarify the relationship between Schmid factor and local strain in the polycrystalline pure Mg and Mg-1.3Y specimens.

speculative. Further investigations using higher-resolution techniques will be required to clarify this point.

Finally, it should be noted that different annealing conditions were employed for pure Mg and the Mg–1.3Y alloy in order to obtain comparable grain sizes, owing to the reduced grain-boundary mobility in the Mg–1.3Y alloy caused by the solute drag effect of Y. As a result, subtle differences in dislocation density, solute distribution, and grain-boundary state may remain between the two materials. Nevertheless, the present study focuses on mesoscopic deformation behavior and strain compatibility at grain boundaries, and the key trends identified here were consistently observed across multiple analyses. Therefore, while such differences cannot be completely excluded, their influence on the main conclusions is considered to be limited.

4. Conclusions

In this study, the relationship between macroscopic tensile properties and mesoscopic local deformation behavior was quantitatively investigated for pure Mg and Mg–1.3Y (at.%) alloys using digital image correlation (DIC) combined with electron backscatter diffraction (EBSD) analysis. The main conclusions are summarized as follows.

(1) Fully recrystallized pure Mg and Mg–1.3Y alloys with comparable equiaxed grain sizes (~25 μm) and strong (0001) basal textures were successfully obtained, enabling a direct comparison of their deformation behavior.
(2) The Mg–1.3Y alloy exhibited superior tensile properties, particularly enhanced ductility, accompanied by a more stable strain-hardening behavior, whereas pure Mg showed a rapid reduction in strain-hardening rate at an early deformation stage.
(3) Both alloys showed similar dominant deformation modes, with basal ⟨a⟩ slip as the primary mechanism and deformation twinning occurring in both materials, suggesting that the difference in ductility cannot be solely attributed to conventional slip or twinning activity.
(4) Pure Mg exhibited pronounced grain-boundary displacement discontinuities and surface step formation, leading to early microcrack-like damage, whereas these features were significantly suppressed in the Mg–1.3Y alloy. This indicates that improved strain compatibility at grain boundaries plays a key role in enhancing ductility.

CRediT authorship contribution statement

Myeong-heom Park: Writing – original draft, Writing – review & editing, Visualization, Methodology, Investigation, Formal analysis, Conceptualization. Binxuan Sun: Investigation, Formal analysis. Saho Yako: Writing – review & editing, Methodology. Akinobu Shibata: Methodology, investigation. Nobuhiro Tsuji: Writing – review & editing, Validation, Supervision, Funding acquisition.

Declaration of competing interest

The authors declare that they have no known competing financial interests or personal relationships that could have appeared to influence the work reported in this paper.

Acknowledgments

This research work was financially supported by JST CREST for Nano-Mechanics (JPMJCR1994), and KAKENHI (Grant-in-Aid for Scientific Research from the Japan Society for the Promotion of Science; JP22K18888, JP23H00234, JP23K20037, JP20K14608, JP24K07214, JP23KJ1268, and JP25K23526), all from the Ministry of Education, Culture, Sports, Science and Technology (MEXT), Japan.

Appendix A. Supplementary data

Supplementary data to this article can be found online at https://doi.org/10.1016/j.jmrt.2026.05.107.

References

[1] Yuan S, Chen X, Pan X, Pan F. Dual-texture induced significant improvement in mechanical properties of extruded ZT31 Mg alloy. Mater Res Lett 2025;13:457–64. https://doi.org/10.1080/21663831.2025.2470886.
[2] Go J, Yako S, Park M-h, Gao S, Lee S, Gholizadeh R. Enhanced strength-ductility balance of AZ31 Mg alloy through single-pass hot-rolling and subsequent low-temperature annealing. 415140639, https://doi.org/10.1016/j.matlet.2026.140639; 2026.
[3] Malik A. Outstanding dynamic tensile response of pure Mg and diluted Mg – mn alloy under very high strain rates. Mater Charact 2025;229:115578. https://doi.org/10.1016/j.matchar.2025.115578.
[4] Somekawa H, Singh A. Tensile response at dynamic strain rates in fine-grained Mg and Mg binary alloys. Mater Sci Eng 2026;953:149745. https://doi.org/10.1016/j.msea.2026.149745.
[5] Masood U, Muhammad H, Tariq R, Zubair M, Ansari N, Jun T. Implications of twinning on the microstructure development, crystallographic texture and mechanical performance of Mg alloys- a critical review. J Magnesium Alloys 2023;11:4146–65. https://doi.org/10.1016/j.jma.2023.09.023.
[6] Go J, Park M-h, Gao S, Tsuji N. Strain localization behavior in a polycrystalline magnesium alloy with de-twinning. Scr Mater 2024;250:116207. https://doi.org/10.1016/j.scriptamat.2024.116207.
[7] Yako S, Park M-h, Tsuji N. Quantitative evaluation of local strain distribution induced by deformation twins and triggering effect of deformation twinning on neighboring grains in polycrystalline AZ31 magnesium alloys. Scr Mater 2025;255:116388. https://doi.org/10.1016/j.scriptamat.2024.116388.
[8] Zhang Z, Yuan L, Ma J, Zheng M, Shan D. Understanding the stress-induced grain boundary migration behavior in a deformed Mg alloy: the role of deformation twin and grain rotation. Int J Plast 2025;185:104244. https://doi.org/10.1016/j.ijplas.2025.104244.
[9] Wang J, Chen Y, Chen Z, Llorca J, Zeng X. Deformation mechanisms of Mg-Ca-Zn alloys studied by means of micropillar compression tests. Acta Mater 2021;217:117151. https://doi.org/10.1016/j.actamat.2021.117151.
[10] Nan X, Wang H, Zhang L, Li J, Jiang Q. Calculation of Schmid factors in magnesium: analysis of deformation behaviors. Scr Mater 2012;67:443–6. https://doi.org/10.1016/j.scriptamat.2012.05.042.
[11] Go J, Park M-h, Gao S, Matsumiya H, Gong W, Tsuji N. Loading-direction dependence of non-basal slip activity in a pre-twinned AZ31 magnesium alloy. J Alloys Compd 2025;1014:178749. https://doi.org/10.1016/j.jallcom.2025.178749.
[12] Go J, Park M-h, Gao SI, Yako S, Tsuji N. Role of detwinning on macroscopic strain localization in magnesium alloy. Metall Mater Trans 2025;56:4377–90. https://doi.org/10.1007/s11661-025-07913-2.
[13] Zhou B, Wang L, Wang J, Maldar A, Zhu G, Jia H, Jin P, Zeng X, Li Y. Dislocation behavior in a polycrystalline Mg-Y alloy using multi-scale characterization and VPSC simulation. J Mater Sci Technol 2022;98:87–98. https://doi.org/10.1016/j.jmst.2021.03.087.
[14] Stanford N, Cottam R, Davis B, Robson J. Evaluating the effect of yttrium as a solute strengthener in magnesium using in situ neutron diffraction. Acta Mater 2014;78:1–13. https://doi.org/10.1016/j.actamat.2014.06.023.
[15] Ogawa Y, Singh A, Somekawa H. Activation of non-basal < c + a > slip in coarse-grained Mg-Sc alloy. Scr Mater 2022;218:114830. https://doi.org/10.1016/j.scriptamat.2022.114830.
[16] Somekawa H, Osawa Y, Singh A, Washio K, Kato A, Mukai T. Effect of micro-alloying elements on deformation behavior in Mg - y binary alloys. Mater Trans 2014;55:182–7. https://doi.org/10.2320/matertrans.M2013303.
[17] Kula A, Jia X, Mishra RAJK, Niewczas M. Mechanical properties of Mg-Gd and Mg-Y solid solutions. Metall Mater Trans B 2016;47:3333–42. https://doi.org/10.1007/s11663-015-0565-x.
[18] Yuan S, Wang J, Zhang L, Jin P. An investigation of the deformation and cracking mechanism of Mg – 1Al – 12Y alloys based on in-situ SEM/EBSD slip trace analysis. Mater Sci Eng 2022;856:144016. https://doi.org/10.1016/j.msea.2022.144016.
[19] Kula A, Jia X, Mishra RK, Niewczas M. Flow stress and work hardening of Mg-Y alloys. Int J Plast 2017;92:96–121. https://doi.org/10.1016/j.ijplas.2017.01.012.
[20] Somekawa H, Basha DA, Singh A. Role of grain boundaries on ductility in Mg-Y alloys. Materialia 2019;8:100466. https://doi.org/10.1016/j.mtla.2019.100466.
[21] Wang S, Wang Y, Ramasse QM, Schmid-fetzer R, Fan Z. Segregation of Yttrium at the Mg/MgO interface in an Mg-0.5Y Alloy. Acta Mater 2023;257:119147. https://doi.org/10.1016/j.actamat.2023.119147.
[22] Robson JD, Haigh SJ, Davis B, Griffiths D. Grain boundary segregation of rare-earth elements in magnesium alloys. Metall Mater Trans 2015;47:522–30. https://doi.org/10.1007/s11661-015-3199-3.
[23] Zhou S, Liu T, Tang A, Shi H, Jing X. Ductility enhancement by activating non-basal slip in Mg alloys with micro-Mn. Trans Nonferrous Met Soc China 2024;34:504–18. https://doi.org/10.1016/S1003-6326(23)66413-1.
[24] Wan X, Yin M, Zeng C, Liu W, Peng P, Zhang L, Jia B. Synergization of yield strength and ductility for a dilute Mg-Zn-Nd-Ca alloy through pinned twin boundary and Guinier – Preston zone. J Magnesium Alloys 2025;13:3466–86. https://doi.org/10.1016/j.jma.2025.04.027.

[25] Zhou S, Liu T, Tang A, Shi H, Chen T. Unveiling the interplay of deformation mechanism in wrought Mg e Sc alloy with different content of manganese. J Mater Res Technol 2022;20:3522–36. https://doi.org/10.1016/j.jmrt.2022.08.091.
[26] Ansari N, Sarvesha R, Yeol S, Singh SS, Jain J. Influence of yttrium addition on recrystallization, texture and mechanical properties of binary Mg – y alloys. Mater Sci Eng 2020;793:139856. https://doi.org/10.1016/j.msea.2020.139856.
[27] Malik A, Nazeer F, Abrar S, Cheng C, Chen Z, Fouda AM. Interfacial bonding, texture evolution, and mechanical properties of different structured extruded Mg-7Gd-4Y-1Zn-0.2Zr and Mg-3Zn-1Al-1Ca-0.5Mn composites. J Magnesium Alloys 2025;13:3373–97. https://doi.org/10.1016/j.jma.2024.07.021.
[28] Zhao L, Zhu X, Xu H, Cheng K, Wang J, Zhao D, Duan J, Sun C, Zhou J, Du Y. Experimental characterization and thermodynamic mapping of grain boundary segregation in Mg-2Y alloy. Materialia 2025;44:102584. https://doi.org/10.1016/j.mtla.2025.102584.
[29] Basha DA, Somekawa H, Singh A. Crack propagation along grain boundaries and twins in Mg and Mg – 0.3 at.%Y alloy during in-situ straining in transmission electron microscope. Scr Mater 2018;142:50–4. https://doi.org/10.1016/j.scriptamat.2017.08.023.
[30] Somekawa H, Basha DA, Singh A, Tsuru T, Yamaguchi M. Non-Basal dislocation nucleation site of solid solution magnesium alloy. Mater Trans 2020;61:1172–5. https://doi.org/10.2320/matertrans.MT-M2020040.
[31] Tasan CC, Hoefnagels JPM, Diehl M, Yan D, Roters F, Raabe D. Strain localization and damage in dual phase steels investigated by coupled in-situ deformation experiments and crystal plasticity simulations. Int J Plast 2014;63:198–210. https://doi.org/10.1016/j.ijplas.2014.06.004.
[32] Park M-h, Gao S, Tsuji N. Grain size-dependent Lüders band dynamics in low-carbon steels: combined insights from digital image correlation and in-situ synchrotron X-ray diffraction. Mater Sci Eng 2025;947:149288. https://doi.org/10.1016/j.msea.2025.149288.
[33] Park M-h, Tagusari Y, Shibata A, Tsuji N. Grain size effects on strain localization and fracture behavior in ferrite–martensite dual-phase steels characterized by digital image correlation analysis. J Mater Res Technol 2025;37:2258–70. https://doi.org/10.1016/j.jmrt.2025.06.165.
[34] Herrera-Solaz V, Patriarca L, Foletti S, Segurado J, Niffenegger M. Microstructure-based modelling and Digital Image Correlation measurement of strain fields in austenitic stainless steel 316L during tension loading. Mater Sci Eng 2019;751:99–106. https://doi.org/10.1016/j.msea.2019.02.063.
[35] Yan D, Tasan CC, Raabe D. High resolution in situ mapping of microstrain and microstructure evolution reveals damage resistance criteria in dual phase steels. Acta Mater 2015;96:399–409. https://doi.org/10.1016/j.actamat.2015.05.038.
[36] Joo SH, Lee JK, Koo JM, Lee S, Suh DW, Kim HS. Method for measuring nanoscale local strain in a dual phase steel using digital image correlation with nanodot patterns. Scr Mater 2013;68:245–8. https://doi.org/10.1016/j.scriptamat.2012.10.025.
[37] Park M-h, Hwang S, Okitsu Y, Tsuji N. Unusual deformation behavior and the consequent emergence of Type C serrations in Fe-1.6Mn-2Ni-1.4Si-0.4C steels. Scr Mater 2025;259:116563. https://doi.org/10.1016/j.scriptamat.2025.116563.
[38] Park M-h, Shibata A, Harjo S, Tsuji N. Grain refinement of dual phase steel maximizes deformation ability of martensite, leading to simultaneous enhancement of strength and ductility. Acta Mater 2025;292:121061. https://doi.org/10.1016/j.actamat.2025.121061.
[39] Chen W, Li X, He W, Jiang B, Pan F. Achieving excellent ductility with increased Schmid Factor but decreased direct strain contribution of basal slip in an intergranular misorientation tailored magnesium alloy. Acta Mater 2025;284:120618. https://doi.org/10.1016/j.actamat.2024.120618.
[40] Shiozawa K, Morii Y, Nishino S, Lu L. Subsurface crack initiation and propagation mechanism in high-strength steel in a very high cycle fatigue regime. Int J Fatig 2006;28:1521–32. https://doi.org/10.1016/j.ijfatigue.2005.08.015.
[41] Shibata A, Matsuoka T, Ueno A, Tsuji N. Fracture surface topography analysis of the hydrogen-related fracture propagation process in martensitic steel. Int J Fract 2017;205:73–82. https://doi.org/10.1007/s10704-017-0182-6.
[42] Zeng ZR, Zhu YM, Xu SW, Bian MZ, Davies CHJ, Birbilis N, Nie JF. Texture evolution during static recrystallization of cold-rolled magnesium alloys. Acta Mater 2016;105. https://doi.org/10.1016/j.actamat.2015.12.045.
[43] Li X, Li X, Zhu J, Ye X, Tang G. Microstructure and texture evolution of cold-rolled Mg-3Al-1Zn alloy by electropulse treatment stimulating recrystallization. Scr Mater 2016;112:23–7. https://doi.org/10.1016/j.scriptamat.2015.09.001.
[44] Nakata T, Kamado S. Towards tailoring basal texture of rolled Mg alloy sheet by recrystallization for high room-temperature formability: a review. J Magnesium Alloys 2023;11:3992–4010. https://doi.org/10.1016/j.jma.2023.08.006.
[45] Somekawa H, Naito K, Watanabe H. Grain boundary relaxation behavior in meso-grained dilute magnesium alloys. Materialia 2020;14. https://doi.org/10.1016/j.mtla.2020.100947.
[46] Sandlo S, Zaefferer S, Schestakow I, Yi S, Gonzalez-martinez R. On the role of non-basal deformation mechanisms for the ductility of Mg and Mg – y alloys. Acta Mater 2011;59:429–39. https://doi.org/10.1016/j.actamat.2010.08.031.
[47] Li W, Wang L, Zhou B, Liu C, Zeng X. Grain-scale deformation in a Mg−0.8 wt % Y alloy using crystal plasticity finite element method. J Mater Sci Technol 2019;35:2200–6. https://doi.org/10.1016/j.jmst.2019.04.030.
[48] Nie JF, Shin KS, Zeng ZR. Microstructure, deformation, and property of Wrought magnesium alloys. Metall Mater Trans 2020;51A:6045–109. https://doi.org/10.1007/s11661-020-05974-z.
[49] Cui Y, Guo L, Gui Y, Aoyagi K, Tong H, Wei Q, Liu F, Hayasaka Y, Chiba A. Segregation behaviors in {10-11} compressive twin boundaries of Mg-RE alloy under deformation at room temperature. J Magnesium Alloys 2025;13:330–7. https://doi.org/10.1016/j.jma.2024.05.023.
[50] Kwon H, Mabuchi M, Chino Y. Microstructure and mechanical properties of alternately-compressed AZ31 Mg alloy in two orthogonal directions. Mater Trans 2014;55:739–41. https://doi.org/10.2320/matertrans.MBW201305.
[51] Sandlöbes S, Friák M, Neugebauer J, Raabe D. Basal and non-basal dislocation slip in Mg–Y. Mater Sci Eng 2013;576:61–8. https://doi.org/10.1016/j.msea.2013.03.006.
[52] Takemoto K, Rikihisa H, Tsushida M, Kitahara H, Ando S. Effects of yttrium addition on plastic deformation of rolled magnesium. Mater Trans 2020;61:935–40. https://doi.org/10.2320/matertrans.MT-M2019384.
[53] Somekawa H, Basha DA, Singh A, Tsuru T, Yamaguchi M. Non-Basal dislocation nucleation site of solid solution magnesium alloy. Mater Trans 2020;61:1172–5. https://doi.org/10.2320/matertrans.MT-M2020040.
[54] Staroselsky A, Anand L. A constitutive model for hcp materials deforming by slip and twinning: application to magnesium alloy AZ31B. Int J Plast 2003;19:1843–64. https://doi.org/10.1016/S0749-6419(03)00039-1.
[55] Koike J, Kobayashi T, Mukai T, Watanabe H, Suzuki M. The activity of non-basal slip systems and dynamic recovery at room temperature in fine-grained AZ31B magnesium alloys. Acta Mater 2003;51:2055–65. https://doi.org/10.1016/S1359-6454(03)00005-3.
[56] Li H, Liu M, Xu T, Zhang R. Super-ductile magnesium alloy at room temperature. Acta Mater 2026;305:121884. https://doi.org/10.1016/j.actamat.2025.121884.
[57] Hauser FE, Starr CD, Tietz LS, Dorn JE. Deformation mechanisms in polycrystalline aggregates of magnesium. Transactions of ASM 1955;47:102–34.
[58] Zheng R, Du JP, Gao S, Somekawa H, Ogata S, Tsuji N. Transition of dominant deformation mode in bulk polycrystalline pure Mg by ultra-grain refinement down to sub-micrometer. Acta Mater 2020;198:35–46. https://doi.org/10.1016/j.actamat.2020.07.055.
[59] Barrett CD, Imandoust A, Kadiri H El. The effect of rare earth element segregation on grain boundary energy and mobility in magnesium and ensuing texture weakening. Scr Mater 2018;146:46–50. https://doi.org/10.1016/j.scriptamat.2017.11.004.
[60] Wu J, Shi Q, Chiu YL. Fragmentation of $Mg_{24}Y_5$ intermetallic particles in an Mg-Zn-Y alloy during the equal channel angular pressing. Mater Charact 2017;129:46–52. https://doi.org/10.1016/j.matchar.2017.04.016.
[61] Nie JF, Muddle BC. CHARACTERISATION OF STRENGTHENING PRECIPITATE PHASES IN A mg–y–nd ALLOY. Acta Mater 2000;48:1691–703. https://doi.org/10.1016/S1359-6454(00)00013-6.
[62] Zhang M, Kelly PM. Morphology and crystallography of $Mg_{24}Y_5$ precipitate in Mg–Y alloy. Scr Mater 2003;48:379–84. https://doi.org/10.1016/S1359-6462(02)00457-8.